Fuel 405 (2026) 136494

Contents lists available at ScienceDirect

Fuel

journal homepage: www.elsevier.com/locate/jfue

Full length article

The interaction between particle clustering and iron particle cloud combustion in homogeneous isotropic turbulence

Gabriel Thäter[a,*], Maurizio Carbone[b], Oliver T. Stein[c], Bettina Frohnapfel[a]

[a] Institute of Fluid Mechanics, Karlsruhe Institute of Technology, Kaiserstraße 10, 76131, Karlsruhe, Germany
[b] Istituto dei Sistemi Complessi, CNR, Via dei Taurini 19, 00185, Rome, Italy
[c] Engler-Bunte-Institute - Chair for Simulation of Reacting Thermo-Fluid Systems, Karlsruhe Institute of Technology, Engler-Bunte-Ring 7, 76131, Karlsruhe, Germany

HIGHLIGHTS

- In iron particle cloud combustion, clustering increases the overall combustion time.
- Iron particles outside clusters ignite later but burn out faster due to the availability of more oxygen.
- Even for equivalence ratios well below one, local oxygen depletion slows down overall reaction.
- The consumption of oxygen leads to locally negative divergence which enhances existing particle clusters.

GRAPHICAL ABSTRACT

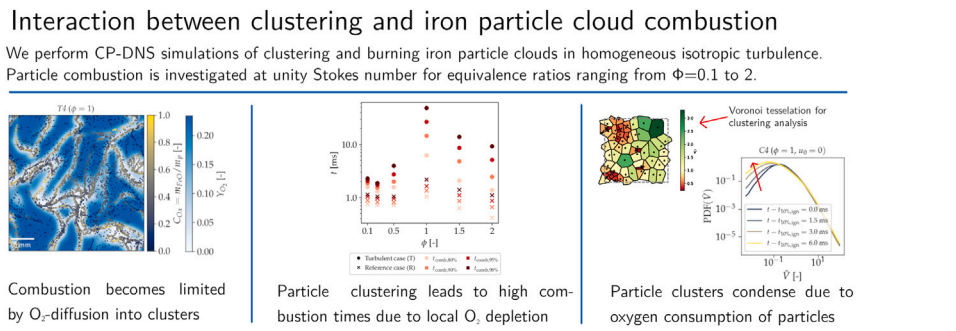

ARTICLE INFO

Keywords:
Iron particle cloud combustion
CP-DNS
Particle clustering
Stokes number
HIT

ABSTRACT

We perform carrier-phase direct numerical simulations (CP-DNS) to investigate the interaction of iron particle cloud combustion and clustering through turbulence. A pseudo spectral multi-phase solver in combination with a point particle iron reaction model is used, capturing mass, heat and momentum transfer between the phases. We investigate the combustion of 10 µm-sized iron particles with air, in homogeneous isotropic turbulence (HIT) at Stokes number one, varying the equivalence ratios from lean (ϕ = 0.1) to fuel-rich (ϕ = 2). At the start, the particles are homogeneously distributed with a temperature below particle ignition temperature. Particle clusters form through turbulence and ignite. While in the very lean regime ($\phi < 0.25$) the O_2 diffusion through the particle boundary layer limits the conversion of Fe to FeO, for $\phi > 0.5$, the oxygen depletion in clusters slows down the overall oxidation progress, and the conversion is limited by the transport of oxygen from regions devoid of particles into clusters. This observation from numerical simulation is supported by a time-scale analysis of the effects involved. We also quantify particle clustering through a Voronoi tessellation and show that through combustion, particle clusters become more prominent. This is caused by two effects. First, if the reacting particles are spaced closely enough to create a local lack of oxygen, a fluid flow is triggered from the regions devoid of particles into clusters. This flow carries particles into the cluster region. Second, finite-size particles cannot follow the fast thermal fluid expansion caused by the exothermic particle reaction as well as the slower compression through heat losses to colder areas.

* Corresponding author.
Email address: gabriel.thaeter@kit.edu (G. Thäter).

https://doi.org/10.1016/j.fuel.2025.136494
Received 13 March 2025; Received in revised form 28 June 2025; Accepted 6 August 2025
Available online 8 September 2025

1. Introduction

The rising energy demand and transition towards renewable sources create the need for large-scale energy storage and long-distance transportation solutions. A promising concept is a redox cycle based on metal fuels. Since both the metal and its oxides are in solid form under ambient conditions, the fuel is kept within the cycle [1,2].

Iron is one of the proposed materials, which can be burned as a powder in air similar to solid carbon-based fuels. Existing coal power plants could be refitted with iron combustion chambers [3]. Unlike volatile-containing carbon-based fuels, the reaction of iron to its oxides occurs mostly in solid or liquid form due to very high boiling temperatures. Therefore, the effects of fluid motion on combustion properties, such as quenching and flame speed, differ from the well-known fuel types. Many experimental and numerical works characterize the combustion of single particles under various conditions [4–6], and several reduced-order models describe the essential aspects of the combustion process through a set of ordinary differential equations [7–11]. These models are crucial to simulate flows involving a large number of particles [12–14]. While some combustion setups allow for self-supporting laminar iron dust flames [15], stabilizing a turbulent flame at industrial scale remains a challenge. Thus, turbulence is still an essential feature of combustion, which becomes important for the transition towards large-scale applications. Despite an increasing number of studies analyzing various cloud combustion conditions e.g. [15–17] the interplay between turbulence, particle motion, and combustion is not yet entirely understood.

It is known that inertial particles form clusters in turbulence [18–20], accumulating preferentially in strain-dominated flow regions [21–23]. This has been observed in simulations of a turbulent mixing layer with reacting iron particles [14,24]. However, the large number of mechanisms at a play, such as the unsteadiness of the shear layer, the anisotropy of the flow, and the particle size distribution, make it difficult to narrow down the influence of particle preferential concentration on the combustion process.

In a recent work, we showed that for initially kinetically-limited particle/air mixtures in homogeneous isotropic turbulence (HIT), ignition occurs first within particle clusters [25]. Now we extend the focus beyond the point of ignition and address the following two questions:

- How does clustering affect the combustion time of iron particles at different equivalence ratios?
- Does combustion influence particle clusters?

2. Modeling and numerical setup

We carry out numerical simulations of iron particle combustion in a turbulent flow through an Eulerian-Lagrangian carrier-phase DNS approach with a point-particle approximation. The velocity field u_i advects two active scalar fields, namely the volumetric enthalpy ρh and oxygen species ρY_{O_2}, together with the reacting inertial particles. The fluid phase simulation relies on a Fourier pseudo-spectral method and is coupled with the particle phase through the Non-Uniform Fast Fourier Transform, while a second-order Runge-Kutta scheme is used for time integration [25,26]. To simulate the iron particle combustion we employ the first-order surface kinetics model (FOSK) [11]. The particles can have a velocity and temperature difference with respect to the surrounding fluid resulting in a two-way heat, mass and momentum transfer. The large density ratio between the particles and the gas phase, up to four orders of magnitude, justifies the assumption of a zero-dimensional particle model. In the following subsections, we describe the modeling in greater detail.

2.1. Thermodynamic fluid model

The fluid phase consists of a mixture of the two ideal gases, oxygen O_2 and nitrogen N_2, governed by the state equation $p_0 = \rho R_M T$, where $p_0(t)$ is the thermodynamic pressure, $\rho(\vec{x},t)$ and $T(\vec{x},t)$ the fluid density and temperature, and $R_M(\vec{x},t) = Y_{\mathrm{O}_2} R_{\mathrm{O}_2} + Y_{\mathrm{N}_2} R_{\mathrm{N}_2}$ the local gas constant of the mixture, with $Y_{\mathrm{O}_2}(\vec{x},t)$ and $Y_{\mathrm{N}_2}(\vec{x},t)$ the local mass fractions of each species. Material properties of the gas are computed from the local temperature, species mass fractions and pressure p_0. In particular, the heat capacity c_p and the specific enthalpy h of the mixture are polynomial functions of the temperature T [27] and the mass fractions of each species Y_{O_2} and Y_{N_2}. For the thermal conductivity λ, we use the empirical relation $\lambda/c_p = 2.58 \times 10^{-5}\,\mathrm{kg\,m^{-1}\,s^{-1}}(T/298\,\mathrm{K})^{0.7}$ introduced in [28]. The dynamic viscosity μ of the fluid and the oxygen mass diffusivity D_{O_2} are determined from the Prandtl and Schmidt (Pr = Sc = 0.7) number definitions,

$$\mu = \mathrm{Pr}\,\frac{\lambda}{c_p} \qquad D_{\mathrm{O}_2} = \frac{\lambda \mathrm{Pr}}{c_p \rho \mathrm{Sc}_{\mathrm{O}_2}}. \tag{1}$$

2.2. Fluid flow

We expect small flow velocities compared to the local speed of sound and therefore apply the low Mach number approximation $p(\vec{x},t) = p_0(t) + \pi(\vec{x},t)$ [29] to the pressure field $p(\vec{x},t)$. The pressure fluctuations π due to momentum changes are small compared to the thermodynamic pressure p_0. The material parameters of the fluid depend on the spatially constant thermodynamic pressure $p_0(t)$, while the fluid momentum Eq. (2c) only features the local pressure fluctuations $\pi(\vec{x},t)$. The governing equations for the gas phase in index notation read

$$\frac{\partial \rho}{\partial t} + \frac{\partial(\rho u_i)}{\partial x_i} = S_{\mathrm{O}_2} \tag{2a}$$

$$\frac{\partial(\rho Y_{\mathrm{O}_2})}{\partial t} + \frac{\partial(\rho u_i Y_{\mathrm{O}_2})}{\partial x_i} = \frac{\partial}{\partial x_i}\left(\rho D_{\mathrm{O}_2} \frac{\partial Y_{\mathrm{O}_2}}{\partial x_i}\right) + S_{\mathrm{O}_2} \tag{2b}$$

$$\frac{\partial(\rho u_i)}{\partial t} + \frac{\partial(\rho u_i u_j)}{\partial x_j} = -\frac{\partial \pi}{\partial x_i} + \frac{\partial \tau_{ij}}{\partial x_j} + S_{i,u} + f_i \tag{2c}$$

$$\frac{\partial H}{\partial t} + \frac{\partial(u_i H)}{\partial x_i} = \frac{\partial}{\partial x_i}\left(\lambda \frac{\partial T}{\partial x_i}\right) + \frac{\mathrm{d}p_0}{\mathrm{d}t} + S_H, \tag{2d}$$

where $u_i(\vec{x},t)$ are the Cartesian components of the fluid velocity, repeated indices imply summation, and $H(\vec{x},t) = \rho h$ is the volumetric enthalpy with units $\mathrm{J\,m^{-3}}$. The external forcing $f_i(\vec{x},t)$ introduces an energy flux into the large flow scales, compensating the small scale dissipation and sustaining turbulence [30]. The stress tensor in Eq. (2) is given by

$$\tau_{ij} = \mu\left(\frac{\partial u_i}{\partial x_j} + \frac{\partial u_j}{\partial x_i} - \frac{2}{3}\delta_{ij}\frac{\partial u_k}{\partial x_k}\right), \tag{3}$$

while the source terms $S_\alpha(\vec{x},t)$ represent the mass, momentum and heat transfer from the particles to the fluid phase. Within the point-particle approximation, they are a superposition of Dirac delta functions centered at the particle positions

$$S_{\mathrm{O}_2} = -\sum_{p=1}^{N_P} \frac{\mathrm{d}m_{\mathrm{O}_2}}{\mathrm{d}t}\delta(\vec{x} - \vec{x}_p) \tag{4a}$$

$$S_{\mathrm{i,u}} = -\sum_{p=1}^{N_P}\left(F_{i,\mathrm{drag}} + \frac{\mathrm{d}m_{\mathrm{O}_2}}{\mathrm{d}t}u_i\right)\delta(\vec{x} - \vec{x}_p) \tag{4b}$$

$$S_{\mathrm{H}} = -\sum_{p=1}^{N_P}\left(\dot{Q}_{\mathrm{conv}} + \dot{Q}_{\mathrm{d}m_p/\mathrm{d}t}\right)\delta(\vec{x} - \vec{x}_p), \tag{4c}$$

where $\mathrm{d}m_{\mathrm{O}_2}/\mathrm{d}t$ is the consumption rate of O_2 mass by the particles and $F_{i,\mathrm{drag}}$ represents the drag force exerted on the particle. The particles alter the fluid enthalpy via convective heat transfer $\dot{Q}_{\mathrm{conv}}$ and mass transfer $\dot{Q}_{\mathrm{d}m_p/\mathrm{d}t}$.

2.3. Iron particle model

As an iron particle combustion model, we use the first-order surface kinetics (FOSK) formulation by Mich et al. [11]. The model considers the reaction of Fe with oxygen to FeO, while neglecting later oxidation stages since they release considerably less energy. Particle melting and solidification plateaus during heat-up and cool-down are captured. The temperature within the particle is assumed to be homogeneous owing to a low Biot number of the particle. The thermodynamic parameters of Fe and FeO are computed as in [11]. The particle temperature follows from the particle enthalpy, total and iron mass through the Shomate equation with parameters from Ref. [31].

The particle state is completely described by the total particle mass m_p, iron mass $m_{p,\mathrm{Fe}}$ and enthalpy H_p, for which the governing equations are

$$\frac{\mathrm{d}m_p}{\mathrm{d}t} = \rho_f Y_{\mathrm{O}_2}|_{\vec{x}_p} A_d k_d \mathrm{Da}^* \tag{5a}$$

$$\frac{\mathrm{d}m_{p,\mathrm{Fe}}}{\mathrm{d}t} = -\frac{1}{s}\frac{\mathrm{d}m_p}{\mathrm{d}t} \tag{5b}$$

$$\frac{\mathrm{d}H_p}{\mathrm{d}t} = \dot{Q}_{\mathrm{conv}} + \dot{Q}_{\mathrm{rad}} + \dot{Q}_{\mathrm{d}m_p/\mathrm{d}t} \tag{5c}$$

$$= -k_c A_p \left(T_p - T|_{\vec{x}_p}\right) + \dot{Q}_{\mathrm{rad}} + \frac{\mathrm{d}m_p}{\mathrm{d}t} h_{\mathrm{O}_2}(T_p). \tag{5d}$$

The subscript p denotes particle variables, while $|_{\vec{x}_p}$ denotes fluid variables evaluated at the particle position. The subscript f indicates the evaluation at film temperature, defined as $T_f = (T|_{\vec{x}_p} + 2T_p)/3$, e.g. the gas film density ρ_f. The normalized Damköhler number is $\mathrm{Da}^* = (A_r k_r)/(A_r k_r + A_d k_d)$, with the reactive and diffusive surface equal to the particle surface area $A_r = A_d = A_p = 4\pi r_p^2$. The kinetic limitation is given by the Arrhenius term $k_r = k_\infty \exp(-T_a/T)$. The radiative heat loss $\dot{Q}_{\mathrm{rad}} = -\epsilon_{\mathrm{rad}}\sigma A_p T_p^4$ is calculated with the emissivity of the particle $\epsilon_{\mathrm{rad}} = 0.7$ and the Boltzmann constant σ. The enthalpy of the oxygen added through the mass transfer is $h_{\mathrm{O}_2}(T_p)$. The diffusive and convective transfer coefficients, $k_d = \mathrm{Sh}^* D_{\mathrm{O}_2,f}/d_p$ and $k_c = \mathrm{Nu}^* \lambda_f/d_p$ follow from the Sherwood and Nusselt numbers, calculated with the Ranz-Marshall fit $\mathrm{Sh} = \mathrm{Nu} = 2 + 0.6\mathrm{Pr}^{1/3}\mathrm{Re}_p^{1/2}$ [32]. The particle Reynolds number is $\mathrm{Re}_p = \rho|_{\vec{x}_p}\|\vec{u}_p - \vec{u}|_{\vec{x}_p}\|d_p/\mu|_{\vec{x}_p}$. Both numbers are corrected to account for the Spalding heat and mass transfer numbers B_M and B_T,

$$\mathrm{Sh}^* = \mathrm{Sh}\frac{\ln(1+B_M)}{B_M}, \qquad \mathrm{Nu}^* = \mathrm{Nu}\frac{\ln(1+B_T)}{B_T}. \tag{6}$$

The Spalding numbers are defined in [11], and all model parameters are taken from there unless stated otherwise.

The particle momentum balance considers the drag force and the momentum exchange due to mass flux between the particle and the gas phase

$$\frac{\mathrm{d}u_{i,p}}{\mathrm{d}t} = \frac{F_{i,\mathrm{drag}} + F_{i,\mathrm{d}m_p/\mathrm{d}t}}{m_p} \tag{7}$$

$$= \frac{u_i|_{\vec{x}_p} - u_{i,p}}{m_p}\left(3\pi\mu d_p(1 + 0.15\mathrm{Re}_p^{0.687}) + \frac{\mathrm{d}m_p}{\mathrm{d}t}\right). \tag{8}$$

3. Computational setup

The simulation domain is a cube with side length L and periodic boundary conditions in all directions. Since the overall mass within the domain is conserved, the thermodynamic pressure $p_0(t)$ will rise during the combustion simulation in HIT. However, pressure does not have a direct influence on particle combustion for the present case. Different from gas flames with direct integration of (pressure-dependent) homogeneous chemistry we do not need to consider gas chemistry for heterogeneously burning iron-air flames. Moreover, since both the thermal transfer coefficient $k_c = \mathrm{Nu}^* \lambda_f/d_p$ of the particle and the term relevant for the oxygen flux ($\mathrm{d}m_p/\mathrm{d}t$) to the particle $\rho_f k_d = \rho_f \mathrm{Sh}^* D_{\mathrm{O}_2,f}/d_p = \mathrm{Sh}^*(\lambda/c_p)_f \mathrm{Pr}/(\mathrm{Sc}_{\mathrm{O}_2} d_p)$ are independent of p_0, the heterogeneous particle reaction rate is therefore not affected by pressure. For a simulation with constant pressure, commonly used for simulating unconfined laboratory burners, the gas density would decrease during combustion. While this would influence absolute particle combustion times, the relative comparison of the cases shown here would still hold.

But a strong influence on particle combustion properties like the burnout time is not expected for our model. A pressure constant in time is not possible for HIT setups with periodic boundaries. Even if the combustion time of a particle does differ due to e.g. different diffusivities within the gas phase, the comparison between the different cases presented in this work still provides valuable insights.

Particle clustering in isotropic turbulence is known to be most prominent at a Stokes number

$$\mathrm{St} = \frac{\tau_p}{\tau_\eta}, \tag{9}$$

of one, that is, the particle inertia time scale $\tau_p = m_p/(3\pi\mu d_p)$ is close to the Kolmogorov time $\tau_\eta = \sqrt{\langle\nu\rangle/\epsilon}$ [18–20]. Here, $\langle\nu\rangle$ is the spatial average of the kinematic viscosity and ϵ corresponds to the mean dissipation rate

$$\epsilon = \frac{1}{\langle\rho\rangle}\left\langle\frac{\partial u_i}{\partial x_j}\tau_{ij}\right\rangle. \tag{10}$$

Particles in large vortices are ejected from the vortex center and preferentially aggregate in regions with high strain rates. This clustering effect is highest for Kolmogorov Stokes numbers around unity [25].

We perform six simulations of turbulent iron particle cloud combustion at St = 1, changing the fuel equivalence ratios from $\phi = 0.1$ to 2 through the number of particles. In order to start the two-phase simulations in statistically converged isotropic turbulent fields, the fluid phase is evolved for more than 25 eddy turnover times without particles settling to a Taylor-scale Reynolds number $\mathrm{Re}_\lambda = \langle u_i u_i\rangle\sqrt{5/(3\langle\nu\rangle\epsilon)} = 41$ and integral scale Reynolds number $\mathrm{Re}_{\ell_{t=0}} = \ell_{t=0}\sqrt{\langle u_i u_i\rangle/3}/\langle\nu\rangle = 66$. $\ell_{t=0}$ is the integral length scale determined by integrating the autocorrelation function of the turbulent velocity field [33]. The enthalpy and oxygen species fields are initialized as constant, only the particle-gas coupling introduces changes to those scalars. At the start of the two-phase simulations, iron particles with $d_{p,0} = 10$ µm are introduced to the domain using a spatially homogeneous random distribution. The initial particle velocity and temperature match the fluid values at the particle position. These cases involving turbulent flow are referred to as *(T1-6)*. In order to compare the turbulent combustion to a case where no forced fluid flow and no particle clustering are present, we performed six additional reference runs *(R1-6)*, starting with zero initial velocity and setting the fluid momentum forcing term f_i in Eq. (2c) to zero. The other parameters are unchanged. The results for cases (R) are very similar to single particles burning with zero slip velocity. While in simulations *(T)*, the turbulent flow drives intense particle clustering, in cases *(R)* fluid flow is driven by the particle feedback only, leading to overall very little fluid motion due to the homogeneous particle distribution. For *(T)*, a particle-induced flow is present where clusters persist, which is expected to be smaller in terms of magnitude compared to the overall turbulent motion of the gas.

As the simulation begins, the particles first oxidize limited by kinetics and slowly heat up before ignition occurs at a particle temperature of ~850 K. This preheating time decreases for higher ϕ, since the overall energy output scales with the number of particles N_p. Throughout this time, turbulence leads to the formation of particle clusters, and in our simulations, the clustering level does not change significantly after 10 Kolmogorov time scales $\sim 10\tau_\eta = 12$ ms. We lower the starting temperature for higher equivalence ratios to ensure a converged particle distribution before ignition. For decreasing temperatures, the dissipation rate $\epsilon_{\mathrm{prerun}} = \mu/(\rho\tau_\eta^2)$ needs to be smaller to keep St = 1. Tables 1 and 2 summarize the simulation parameters.

Table 1
Common parameters for all simulations.

Variable	Value	
N	64	Number of resolved Fourier modes
Δt	3×10^{-6} s	Time step
$k_{\max}$	$\sqrt{3}\frac{2\pi}{L}\,\mathrm{m}^{-1}$	Maximum forced wave number (cases *(T1–6)*)
$Y_{\mathrm{O}_2,t=0}$	0.233	O_2 mass fraction at $t = 0$
$p_{0,t=0}$	$1 \times 10^5\,\mathrm{N\,m}^{-2}$	Thermodynamic pressure at $t = 0$

Table 2
Parameters specific for each turbulent case *(T)* and reference case *(R)*.

	T1/R1	*T2/R2*	*T3/R3*	*T4/R4*	*T5/R5*	*T6/R6*
ϕ [−]	0.10	0.25	0.50	1.00	1.50	2.00
N_p [−]	0.235 M	0.585 M	1.163 M	2.304 M	3.434 M	4.564 M
L [mm]	29.9	29.8	29.6	29.3	29.1	29.0
$T_{t=0}$ [K]	796.6	789.7	779.7	764.8	754.8	749.8
$\epsilon_{\mathrm{prerun}}$ [$\mathrm{m^2\,s^{-3}}$]	58.3/0	56.7/0	54.5/0	51.2/0	49.1/0	48.1/0
$\ell_{t=0}^{\prime}$ [mm]	6.33	6.30	6.26	6.21	6.17	6.15
$\tau_\eta = \tau_p$ [ms]	1.19	1.20	1.21	1.23	1.24	1.24

The resulting mean particle slip velocities $|u_i - u_{i,p}|$ during the simulation are $\sim 0.25\ \mathrm{m\,s^{-1}}$ with a standard deviation of $\sim 0.1\ \mathrm{m\,s^{-1}}$, which is comparable to recent experimental-numerical work conducted on a 47 kW laboratory burner [34], where slip velocities up to $1\ \mathrm{m\,s^{-1}}$ are reported for particles twice the present size. Compared to laboratory iron-air flames our HIT setup features an increase in pressure with time, does not have any mean shear and only models the first oxidation stage of iron, neglecting the later stages. However, this well-defined setup allows for fundamental investigations of the effects of turbulence, particle clustering and equivalence ratio on iron-air flame characteristics which are the focus of the present study.

4. Results and discussion

We start by investigating the influence of clustering on iron particle cloud combustion in Section 4.1, before looking into the opposite direction in Section 4.2.

4.1. Results of clustering influence on burn time

We define the ignition event of a single particle as the time with the highest temperature gradient $\mathrm{d}T_p/\mathrm{d}t$ of a particle during oxidation. Since the duration from the start of the simulation until the first particles ignite differs between cases, we define a reference time at which 10 % of all particles have ignited as $t_{10\%,\mathrm{ign}}$. Later stated times give the duration past that specified ignition time, namely $t - t_{10\%,\mathrm{ign}}$. Fig. 1 shows 2D slices through the three-dimensional domain at $t - t_{10\%,\mathrm{ign}} = 1.2$ ms. We use the mass fraction $C_{\mathrm{Ox}} = m_{\mathrm{FeO}}/m_p = 1 - m_{\mathrm{Fe}}/m_p$ to quantify the oxidation progress of each particle. At this stage, for the lean setup $\phi = 0.1$, all particles in clusters are burnt out ($C_{\mathrm{Ox}} = 1$), and locally still have gaseous oxygen left. Instead, particles outside clusters have not yet ignited because the heat released by the oxidizing particles has not yet spread to provide heat for ignition. For higher ϕ, the local O_2 concentration in clustered regions tends to zero, and not all particles can quickly burn out. This limiting effect manifests even for the globally lean case with $\phi = 0.5$.

We express the overall combustion progress over time as the fraction of the iron mass converted to oxide,

$$C(t) = 1 - \frac{\sum_{p=1}^{N_P} m_{p,\mathrm{Fe}}(t)}{\sum_{p=1}^{N_P} m_{p,\mathrm{Fe}}(t=0)}. \tag{11}$$

This combustion progress variable starts at 0 for $t = 0$ and reaches a maximum $C_{\max} = \min(1, 1/\phi)$ at late times. Fig. 2 shows the overall combustion time $t_{\mathrm{comb,X\%}} = t_{P,\mathrm{X\%}} - t_{10\%,\mathrm{ign}}$, where t_P is the time at which C is $X\% = 80\,\% \cdots 98\,\%$ of $C_{\max}$. Compared to the reference cases *(R)*, without strongly turbulent fluid motion and particle clustering, the combustion times in a turbulent flow *(T)* are always longer. This is because particles in clusters ignite earlier, but it takes additional time for the heat released in the clustered regions to spread and ignite particles in less populated regions. The turbulent case with $\phi = 1$ has the longest combustion duration. Since neither oxygen nor iron surplus is present in the domain, all oxygen has to be transported to unburnt iron, which is very sparse in the later stages of the simulation. When increasing ϕ past stoichiometry, the combustion time decreases but remains significantly higher than the reference case. In the following, we will characterize the connection between the increase in combustion time and the local particle distribution in greater detail.

To quantify clusters, we perform a 3D Voronoi tessellation [12,35,36], using the Python package freud, based on Voro++ [37,38]. The tessellation divides the 3D space into regions closest to individual particles, based on the local particle number density. The volume V of the Voronoi cells normalized by their spatial average, $\hat{V} = V/\langle V \rangle$, indicates the local clustering level. Particles in dense groups have a smaller $\hat{V}$ than those in void regions, while the mean normalized volume is fixed at $\langle \hat{V} \rangle = 1$.

We run the Voronoi analysis on the particle phase at $t = t_{10\%,\mathrm{ign}}$. Then we sort all particles according to their volume $\hat{V}$. If a particle belongs to the 10 % smallest volumes, it is considered “in a cluster”, if it is within the largest 10 %, it is “outside clusters”. This classification does not account for the strength of the clustering, which is comparable among simulations *(T)* since they have the same reference Stokes number. Also particle groups can break apart, but their lifetime correlates with their size. Larger clusters, at the end of their lifetime, tend to split apart and recombine into new large clusters [39]. Correlating the Voronoi volumes at $t = t_{10\%,\mathrm{ign}}$ with $t - t_{10\%,\mathrm{ign}} = 5$ ms still gives

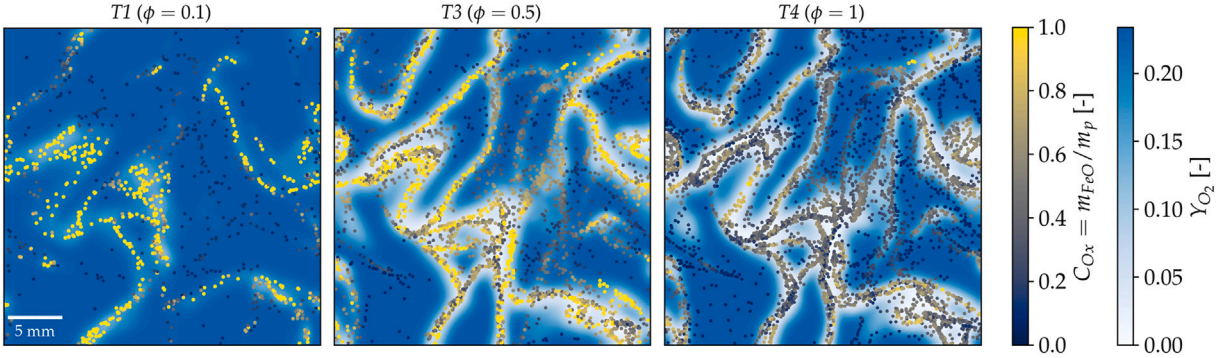

Fig. 1. 2D slices of burning iron particles in HIT. For $\phi > 0.5$, the O_2 inside particle clusters becomes a limiting factor for further oxidation. Particle sizes are exaggerated.

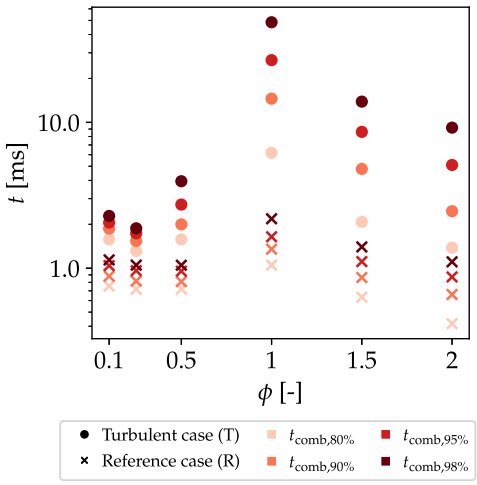

Fig. 2. Time from ignition to end of combustion, defined by the percentage of oxidized iron.

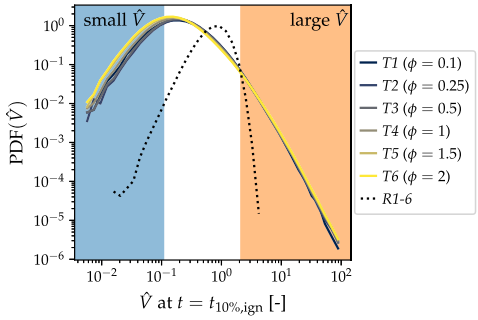

Fig. 3. PDF of Voronoi volumes $\hat{V}$. *T1–T6* are very similar due to identical Stokes numbers. The dotted line shows the distribution for *R1–6*, the colored areas the grouping in- and outside clusters.

a (Pearson) coefficient of 0.5–0.7, depending on the setup. However, at times > 5 ms, the correlation coefficient decreases further, and the categorization made on the initial clustering state tends to apply less. The probability density function for all *(T)* cases $t = t_{10\%,\,ign}$ is in Fig. 3. The PDF of $\hat{V}$ has fat tails corresponding to both small and large $\hat{V}$, compared to the narrower random and homogeneous distribution (dotted line), showing the presence of clustering.

Different clustering levels affect the evolution of the particle combustion. To analyze this, we consider the time evolution of the particle temperature T_p, the oxygen mass fraction at the particle position $Y_{O_2}|_{\vec{x}_p}$ and the oxidation progress C_{Ox}, conditional on the initial clustering level in the vicinity of the particle. In Fig. 4, each row corresponds to the quantity indicated on the left, and each column represents a different turbulent simulation. The blue (orange) lines and areas show the mean and standard deviation of the variables relative to the particles inside (outside) clusters, and the black solid line indicates the mean value over all particles. The temperature plot shows that particles inside clusters ignite earlier than those outside. Within clusters, the particle oxidation for the turbulent case with $\phi = 0.1$ progresses similarly to the reference case (simulations (*R*), dotted line), while low particle concentration leads to delay in the ignition. However, for high ϕ, the local oxygen mass fraction drops more prominently in the clusters, significantly reducing the oxidation rate, which is proportional to $Y_{O_2}|_{\vec{x}_p}$, see Eq. (5a). Particles outside clusters have more available oxygen and burn out faster, as shown by the crossing between the C_{Ox} curves relative to particles inside and outside the clusters for $\phi \geq 0.5$.

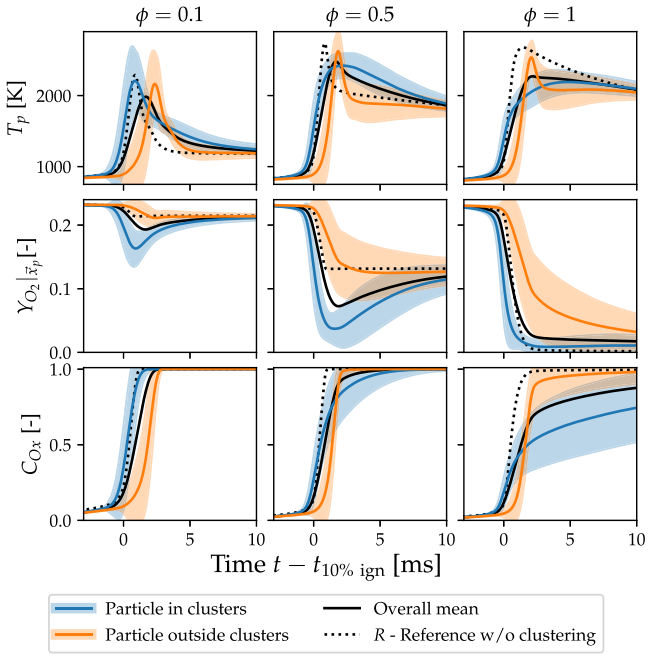

Fig. 4. Particle and fluid quantities over time, averaged over particles in and outside clusters. Rows: Particle temperature T_p, gas oxygen mass fraction $Y_{O_2}|_{\vec{x}_p}$ at particle position $\vec{x}_p$ and oxidation progress $C_{Ox} = m_{FeO}/m_p$.

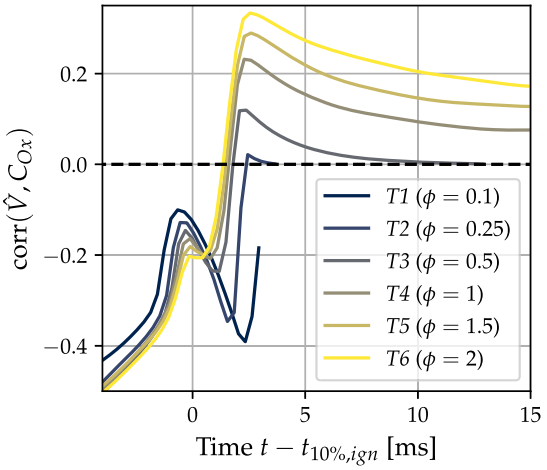

Fig. 5. Correlation between Voronoi volume $\hat{V}$ and oxidation progress C_{Ox} for different equivalence ratios ϕ. Initially, particles in clusters are further oxidized, the correlation is negative. The sign then flips for $\phi > 0.25$, particles outside groups burn out faster.

Particles inside clusters reach lower peak temperatures since a slower oxidation reduces the heat release on the particle.

The local oxygen depletion is more pronounced for high equivalence ratios. For $\phi = 1$, the particles outside the clusters ignite last, but almost all burn out within 2.5 ms. Instead, particles in clusters combust slowly, and even after 10 ms the mean oxidation progress is only 75 %. This shows that the high combustion time shown in Fig. 2 is mainly due to incomplete oxidation within clusters. Even if enough oxygen is available globally, the partially unburnt iron and oxygen are spaced apart, and the combustion rate is limited by the oxygen diffusion from oxygen-rich regions towards oxygen-depleted regions within particle clusters.

Fig. 5 shows the correlation of the oxidation progress C_{Ox} and normalized Voronoi volume $\hat{V}$ over time. Up to the ignition time the value is always negative, so further oxidized particles tend to be close together

with small $\hat{V}$. Already for $\phi = 0.25$, but more pronounced for $\phi > 0.5$, the sign of the correlation flips ~2 ms after ignition, showing that particles with higher C_{Ox} will now be found outside clusters. For $\phi < 1$ the correlation tends to zero and becomes undefined when $C_{\mathrm{Ox}} = 1$ is reached for all particles.

Our results indicate that, for the considered setup, oxygen transport into clusters is rate-limiting for higher ϕ. We now compare the characteristic time scales of diffusion and particle combustion to see whether the limiting mechanism can be estimated through flow and particle parameters. When a single particle is burning in an excess of oxygen at high particle temperatures $T_p > 1500$ K, the Damköhler number Da^* is close to unity, and the overall combustion time $\tau_{p,\mathrm{comb}}$ can be estimated through Eq. (5b) as in [40]

$$\tau_{p,\mathrm{comb}} \approx \frac{m_{p,t=0}}{\left|\frac{\mathrm{d}m_{\mathrm{Fe}}}{\mathrm{d}t}\right|_{t=0}} = \frac{\rho_p \frac{4}{3}\pi r_p^3}{\frac{1}{s}\rho_f Y_{\mathrm{O}_2} A_d k_d} = \frac{1}{3} r_p^2 \, s\rho_{\mathrm{Fe}} \frac{\mathrm{Sc}}{Y_{\mathrm{O}_2}\mu_f}. \tag{12}$$

For a 10 µm-sized iron particle with temperature of 1200 K in air at 800 K, the resulting time scale is $\tau_{p,\mathrm{comb}} = 1.2$ ms, comparable to the Kolmogorov time τ_η, see Table 2. Igniting particles consume the oxygen available in their vicinity, and if the oxygen concentration becomes too low, oxygen needs to be transported from regions in the flow with an excess of O_2 for particles to react further. Oxygen is transported through turbulent and molecular diffusion. The molecular diffusion is proportional to D_{O_2}, while the turbulent diffusion coefficient is scale-dependent. We consider the regime $\phi \gtrsim 1$, where, for the particles to combust, oxygen and particles have to be mixed by the underlying flow over the scale of the characteristic cluster separation length up to the domain size. Particles at St = 1 cluster at the edges of large vortices, resulting in a characteristic separation of clusters of the order of the integral length scale, $\ell \simeq 6.2$ mm. At these large scales, the turbulent transport behaves similarly to molecular diffusion [41]. Neglecting viscous and particle-induced effects in Eq. (2), the associated turbulent diffusion coefficient is estimated as the time integral of the velocity correlation along Lagrangian tracer trajectories, $D_{\mathrm{turb}} = \int_{t=t_0}^{\infty} \langle u_i(\vec{x}(t_0), t_0) u_i(\vec{x}(t), t)\rangle \mathrm{d}t$ [41–43] with $t_0 = t_{10\%,\mathrm{ign}}$. This yields $D_{\mathrm{turb}} \simeq 0.01$ m^2 s^{-1} in our simulations, much higher than the molecular diffusion coefficient $D_{\mathrm{O}_2} \simeq 0.0001$ m^2 s^{-1}. With the integral length scale $\ell \simeq 6.2$ mm and the domain size $L \simeq 29.3$ mm, the time scales of turbulent oxygen diffusion into particle clusters range from $\tau_{D,\ell} = \ell^2/D_{\mathrm{turb}} \simeq 3.8$ ms to $\tau_{D,L} = L^2/D_{\mathrm{turb}} = 86$ ms. Therefore, large-scale oxygen diffusion is slow compared to single-particle combustion ($\tau_{p,\mathrm{comb}} < \tau_{D,\ell} < \tau_{D,L}$), which explains the increase in combustion time observed in Fig. 2 for clustered particles with $\phi \geq 1$ *(T4–6)*. A similar time-scale analysis can be applied to other setups in which oxygen only diffuses into clusters from nearby regions, considering the smaller scale turbulent transport, which will be the subject of future work.

4.2. Influence of particle cloud combustion on clustering

So far we have investigated the influence of clustering on iron particle combustion, now we look into the effect in the opposite direction. The first three subplots in Fig. 6 show the temporal evolution of the Voronoi size distribution for the turbulent cases at $\phi = 0.1$, 0.5 and 1. The left tail of the PDF, related to particle clusters, always increases in the first few ms after ignition.

To separate the influence of the turbulent fluid motion on clustering from the effect of combustion, we use the particle positions of case *(T4)* at $t = t_{10\%,\mathrm{ign}}$ as clustered initial positions, but initially set the fluid and particle velocity to zero ($\vec{u}(t=0) = \vec{u}_p(t=0) = \vec{0}$). The NSE and particle motion are solved as before, only the fluid forcing f_i is turned off for this additional simulation *(C4)*. The particle-fluid coupling still induces fluid motion. The initial conditions are otherwise unchanged compared to *(T4)*.

2D slices of the 3D domain at the time steps $t - t_{10\%,\mathrm{ign}} = 0$ ms, 3 ms and 12 ms are shown in Fig. 7. The clusters remain approximately at the same positions throughout the combustion process because there is no underlying turbulent flow. Similarly to case *(T4)*, the particles in clusters ignite first but need more time to fully oxidize, so at 3 ms, only particles inside groups have $C_{\mathrm{Ox}} < 1$. Comparing the cluster width at the beginning and the width at 12 ms shows that the particle groups contract to almost single lines, indicating an effect of oxidation on clustering. The rightmost plot in Fig. 6, showing the PDF of Voronoi volumes, confirms this clustering enhancement by combustion. The left tail of the PDF, representative of the particles close together, is even more pronounced for simulation *(C4)* than for case *(T4)* which features an underlying turbulent flow.

Due to mass and heat transfer, the particles induce fluid motion. The divergence of the resulting velocity field is shown as the background color in Fig. 7. At 0 ms, the divergence is preferentially positive near particle clusters, indicating fluid expansion, while most fluid in the domain contracts slightly, with $\partial_i u_i < 0$ (we use the abbreviation $\partial_i \equiv \partial/\partial x_i$ for notational simplicity). Later, at 3 ms, the divergence is preferentially negative, whereas the outside regions are expanding. At 12 ms, the divergence has a similar distribution but lower magnitude. In the following subsections, we propose two effects connecting the particle clustering to the divergent fluid motion.

4.2.1. Enhanced clustering through oxygen consumption

Iron particles remain mostly in a solid or liquid phase during combustion, different from hydrocarbon-based fuels such as coal or biomass. Oxygen from the surroundings reacts to form FeO with a density four orders of magnitude higher, thus inducing a Stefan flow to the particle. A single iron particle with mass $m_{p,0} = \rho_{\mathrm{Fe}} d_{p,0}^3 \pi/6$ consumes the oxygen mass $m_{\mathrm{O}_2} = s m_{\mathrm{Fe}}$. We suppose this amount of oxygen is contained in an idealized sphere surrounding the particle with mass $m_{\mathrm{O}_2} = \rho_{\mathrm{O}_2} Y_{\mathrm{O}_2} d_{\mathrm{O}_2}^3 \pi/6$ and diameter

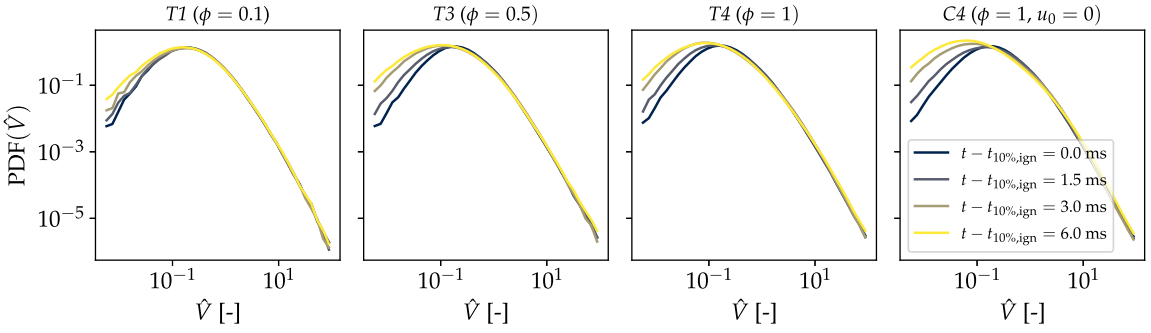

Fig. 6. The evolution of Voronoi volumes over time for different cases. The lower end of the PDF increases since the combustion enhances clusters. *(C4)* is a case with clustered particle positions from *(T4)*, but an initial gas and particle velocity of zero.

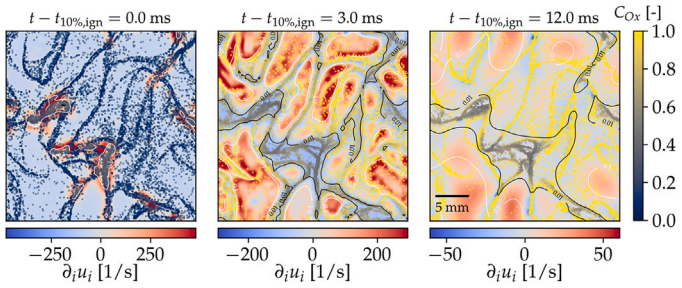

Fig. 7. The fluid velocity divergence $\partial_i u_i = \partial u_i / \partial x_i$ of three slices of the clustered case *(C4)* with $\phi = 1$ and initially a fluid and particle velocity of $u_0 = u_{p,0} = 0$. The clusters collapse, a negative divergence at particle clusters can be seen for later times after ignition. Additionally, isolines of Y_{O_2} are shown.

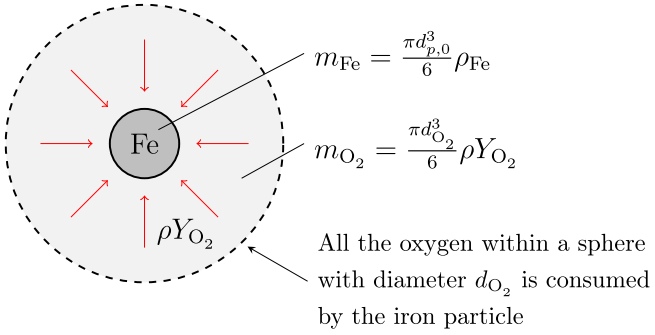

Fig. 8. Sketch of the minimal gas volume affected by the O_2 consumption.

$$d_{O_2} = d_{\mathrm{Fe}} \sqrt[3]{\frac{\rho_{\mathrm{Fe}}}{\rho} \frac{Y_{O_2}}{s}}, \tag{13}$$

as illustrated in Fig. 8. Eq. 13 gives an approximate length scale of the region influenced by a particle. For the chosen simulation parameters, this length becomes $d_{O_2} \simeq 24 d_{p,0} = 240$ µm, comparable to the Kolmogorov scale $\eta = \sqrt{\epsilon \tau_\eta^3} = 310$ µm, see Table 2. For $\phi = 1$ and a homogeneous particle distribution, the mean particle distance is approximately equal to d_{O_2}. But if particles are closer together, the influenced regions overlap, and neighboring particles will approach each other. In Fig. 7, the particle size is exaggerated for better visibility and is roughly half of d_{O_2}. Hence, wherever particles visually overlap in the figure, the resulting fluid flow will reduce the inter-particle distance. In regions with many particles close together at 3 and 12 ms, reacting clusters induce a negative fluid velocity divergence, condensing existing groups. Isolines of Y_{O_2} in Fig. 7 show that for later times, indeed the oxygen depletion correlates with the negative divergence.

4.2.2. Enhanced clustering through fluid expansion/contraction

The heat exchange between the particle and gas phase triggers an expansion or contraction of the fluid. Depending on the time scales, particles may or may not follow this motion. A burning particle releases heat to its close proximity, generating a hot spot in the domain. Following the Low-Mach assumption, the fluid expands as fast as the heat transfer occurs since no local pressure gradient builds up. Therefore the time scale is either the particle combustion time $\tau_{p,\mathrm{comb}}$ or the temperature response time of the particles $\tau_{p,T} = |\Delta T / (\mathrm{d}T/\mathrm{d}t)| = c_{p,p} r_p^2 \rho_p / (3\lambda) = 0.8$ ms [26], both of which can be limiting. With the inertial particle response time $\tau_p = 2 r_p^2 \rho_p / (9\mu)$, a Stokes number for the expansion is defined as

$$\mathrm{St}_{\mathrm{exp}} = \frac{\tau_p}{\max(\tau_{p,T}, \tau_{p,\mathrm{comb}})} \simeq 1. \tag{14}$$

The heat released by the particle is distributed through molecular and turbulent diffusion, and the clustered regions cool down. The thermal contraction in the clusters occurs on the time scale of heat transfer in the fluid to regions without particles, τ_T, which is estimated similarly to Section 4.1 with the turbulent diffusivity D_{turb}. Heat transfer occurs over the length ℓ from clusters to their surroundings, similar to the oxygen diffusion described above. In our setup, we compute the Stokes number for thermal contraction using $\tau_T \simeq \tau_{D,\ell}$ as

$$\mathrm{St}_{\mathrm{con}} = \frac{\tau_p}{\tau_{D,\ell}} = \frac{1.2\ \mathrm{ms}}{3.8\ \mathrm{ms}} \simeq 0.3. \tag{15}$$

Particles with $\mathrm{St} \ll 1$ have a negligible slip velocity, whereas particles with $\mathrm{St} \gg 1$ are mostly uncorrelated with the flow [23]. Since $\mathrm{St}_{\mathrm{exp}} \simeq 1$ and $\mathrm{St}_{\mathrm{con}} < 1$, the particles tend to follow the contracting motion of the fluid more easily. Even though this Stokes analysis is just a qualitative

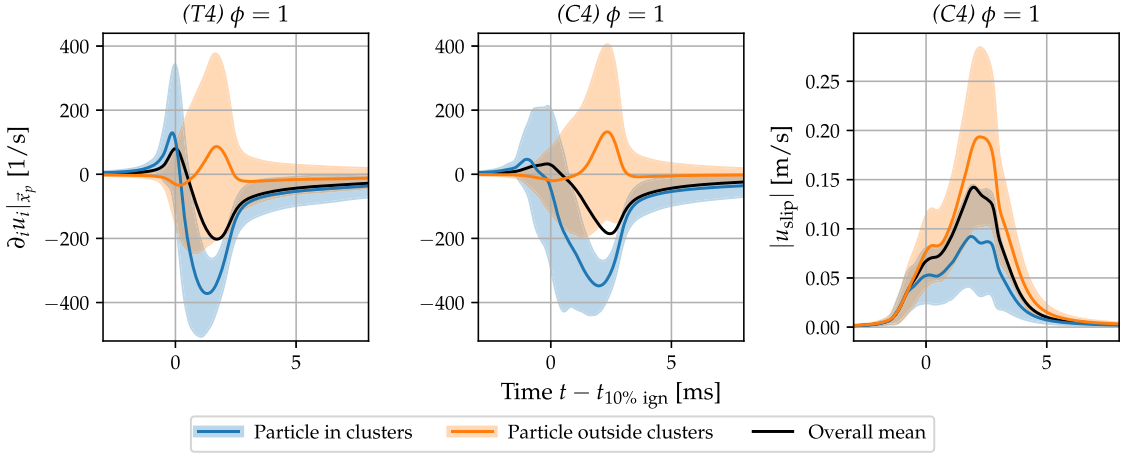

Fig. 9. Fluid divergence $\partial_i u_i = \partial u_i / \partial x_i$ at particle position, averaged over particles in- and outside clusters (blue/orange) and all particles (black). The expansion ($\partial_i u_i > 0$) lasts much shorter than the contraction ($\partial_i u_i < 0$), making the clustering more pronounced. The particle slip velocity $|u_{i,\mathrm{slip}}| = |u_i - u_{i,p}|$ in the right plot shows small values for late times, indicating that particles closely follow the contractive motion of the flow. (For interpretation of the references to colour in this figure legend, the reader is referred to the web version of this article.)

measure, it can be an additional factor for the enhancement of clustering during combustion. However, in the turbulent case (*T*), the slow thermal contraction is concealed by the turbulent motion, which has a shorter time scale $\tau_\eta = \tau_p$, and the thermal effects are weaker than the negative divergence induced by oxygen consumption. This might explain why the clustering level (left tail of the PDF) in Fig. 6 increases more prominently for the zero initial velocity case *(C4)* than for the turbulent case *(T4)*.

Finally, to summarize the effect of the fluid velocity divergence, we examine the divergence at the particle positions $\partial_i u_i|_{\vec{x}_p}$. Fig. 9 shows the mean and standard deviation for clustered and unclustered particles over time for the cases *(T4)* and *(C4)*. Both simulations show a very similar behavior, so the findings from the stationary case *(C4)* also apply to the turbulent one *(T4)*. Particles outside clusters experience a weak initial contraction and then an expansion, consistent with the slices in Fig. 7. Clustered particles are subjected to an initial expansion ($\partial_i u_i > 0$), which only lasts for < 1 ms, comparable to $\tau_p = 1.2$ ms ($\mathrm{St}_{\mathrm{exp}} \simeq 1$). Instead, the fluid contraction reaches higher absolute values and has a longer duration ($\mathrm{St}_{\mathrm{con}} < 1$). This ultimately leads to the contraction of existing clusters. The right subplot in Fig. 9 shows the magnitude of the particle slip $|u_{\mathrm{slip}}| = |u_i - u_{p,i}|$. At times $t > 4$ ms we see very small slip velocities compared to earlier times, indicating that the particles follow the contractive motion of the gas more closely than the brief expansion around $t = 0$ ms.

5. Conclusion

Using Carrier-Phase Direct Numerical Simulations, we investigated igniting and combusting iron particle clouds in homogeneous isotropic turbulence at unity particle Stokes number for a wide range of equivalence ratios. We showed that particle clustering increases the overall combustion time, most pronounced for an equivalence ratio of 1, where it is raised by a factor of 10 compared to a stationary simulation with a homogeneous particle distribution. The rate-limiting factor was found to be the oxygen diffusion into particle clusters, where a lack of oxygen is present. The diffusion time scale based on the spacing between clusters is large compared to the fast particle combustion time for a single particle. Moreover, the combustion condenses already existing clusters. The oxygen consumption by the non-volatile iron particles causes a Stefan flow towards individual particles, which results in a net flow into particle groups with a lack of oxygen, contracting the clusters further due to the negative divergence $\partial u_i/\partial x_i < 0$.

For practical applications, our results show the importance of maintaining homogeneity in particle-air mixtures. If the particle number density is locally higher, either due to turbulent clustering or inhomogeneous particle seeding, particles will take a longer time to burn out completely. The collapsing of clusters increases the otherwise very small probability of particle collisions, which are not captured by our simulation. This is a possible next step for investigation, since it might be disadvantageous for the application of the redox cycle, if molten iron-oxide particles collide and form larger particles.

CRediT authorship contribution statement

Gabriel Thäter: Writing – review & editing, Writing – original draft, Visualization, Validation, Software, Formal analysis. **Maurizio Carbone:** Writing – review & editing, Writing – original draft, Validation, Software, Formal analysis. **Oliver T. Stein:** Writing – review & editing, Supervision, Conceptualization. **Bettina Frohnapfel:** Writing – review & editing, Supervision, Funding acquisition, Conceptualization.

Declaration of competing interest

The authors declare that they have no known competing financial interests or personal relationships that could have appeared to influence the work reported in this paper.

Acknowledgments

This work is conducted within the *Clean Circles* research initiative financially supported by KIT Strategiefonds. In addition, the authors gratefully acknowledge the financial support of the Helmholtz Association of German Research Centers (HGF), within the research field *Energy*, program *Materials and Technologies for the Energy Transition (MTET)*, topic *Resource and Energy Efficiency*. The authors also acknowledge support from the state of Baden-Württemberg through bwHPC and the computing time provided on the high-performance computer HoreKa by the National High-Performance Computing Center at KIT (NHR@KIT). This center is jointly supported by the Federal Ministry of Education and Research and the Ministry of Science, Research and the Arts of Baden-Württemberg, as part of the National High-Performance Computing (NHR) joint funding program (https://www.nhr-verein.de/en/our-partners). HoreKa is partly funded by the German Research Foundation (DFG).

Data availability

The postprocessed data used for the figures is openly available in the KITopen repository at doi: https://doi.org/10.35097/1kvgp3srcuzj1b0h

References

[1] Bergthorson JM, Goroshin S, Soo MJ, Julien P, Palecka J, Frost DL, et al. Direct combustion of recyclable metal fuels for zero-carbon heat and power. Appl Energy 2015;160:368–82.
[2] Neumann J, da Rocha RC, Debiagi P, Scholtissek A, Dammel F, Stephan P, et al. Techno-economic assessment of long-distance supply chains of energy carriers: comparing hydrogen and iron for carbon-free electricity generation. Appl Energy Combust Sci 2023;14:100128.
[3] Janicka J, Debiagi P, Scholtissek A, Dreizler A, Epple B, Pawellek R, et al. The potential of retrofitting existing coal power plants: a case study for operation with green iron. Appl Energy 2023;339:120950.
[4] Ning D, Shoshin Y, van Oijen JA, Finotello G, de Goey LPH. Burn time and combustion regime of laser-ignited single iron particle. Combust Flame 2021;230:111424.
[5] Thijs LC, van Gool CEAG, Ramaekers WJS, van Oijen JA, de Goey LPH. Resolved simulations of single iron particle combustion and the release of nano-particles. Proc Combust Inst 2023;39(3):3551–9.
[6] Deutschmann MP, Sperling A, Covini E, Böhm B, Dreizler A, Nirschl H. Single iron particle combustion – a morphology study of partially oxidized iron particles. Powder Technol 2024;445:120102.
[7] Sidorov AE, Shevchuk VG. Laminar flame in fine-particle dusts. Combust Explos Shock Waves 2011;47(5):518–22.
[8] Soo M, Goroshin S, Bergthorson JM, Frost DL. Reaction of a particle suspension in a rapidly-heated oxidizing gas. Propellants Explos Pyrotech 2015;40(4):604–12.
[9] Hazenberg T, van Oijen JA. Structures and burning velocities of flames in iron aerosols. Proc Combust Inst 2021;38(3):4383–90.
[10] Mi X, Fujinawa A, Bergthorson JM. A quantitative analysis of the ignition characteristics of fine iron particles. Combust Flame 2022;240:112011.
[11] Mich J, Braig D, Gustmann T, Hasse C, Scholtissek A. A comparison of mechanistic models for the combustion of iron microparticles and their application to polydisperse iron-air suspensions. Combust Flame 2023;256:112949.
[12] Weiss P, Bhopalam SR, Meyer DW, Jenny P. On droplets that cluster and evaporate in reactive turbulence. Phys Fluids 2021;33(3):033322.
[13] Rieth M, Kempf AM, Kronenburg A, Stein OT. Carrier-phase dns of pulverized coal particle ignition and volatile burning in a turbulent mixing layer. Fuel 2018;212:364–74.
[14] Luu TD, Shamooni A, Kronenburg A, Braig D, Mich J, Nguyen B-D, et al. Carrier-phase dns study of particle size distribution effects on iron particle ignition in a turbulent mixing layer. Proc Combust Inst 2024;40(1):105297.
[15] Fedoryk M, Stelzner B, Harth S, Trimis D. Experimental investigation of the laminar burning velocity of iron-air flames in a tube burner. Appl Energy Combust Sci 2023;13:100111.
[16] Goroshin S, Tang F-D, Higgins AJ. Reaction-diffusion fronts in media with spatially discrete sources. Phys Rev E 2011;84(2):027301.
[17] Palečka J, Goroshin S, Higgins AJ, Shoshin Y, de Goey P, Angilella J-R, et al. Percolating reaction–diffusion waves (perwaves)—sounding rocket combustion experiments. Acta Astronaut 2020;177:639–51.
[18] Eaton JK, Fessler JR. Preferential concentration of particles by turbulence. Int J Multiphase Flow 1994;20:169–209.
[19] Bec J, Biferale L, Cencini M, Lanotte A, Musacchio S, Toschi F. Heavy particle concentration in turbulence at dissipative and inertial scales. Phys Rev Lett 2007;98(8):084502.
[20] Bec J, Gustavsson K, Mehlig B. Statistical models for the dynamics of heavy particles in turbulence. Annu Rev Fluid Mech 2024;56:189–213.
[21] Wang L-P, Maxey MR. Settling velocity and concentration distribution of heavy particles in homogeneous isotropic turbulence. J Fluid Mech 1993;256:27–68.
[22] Bragg AD, Ireland PJ, Collins LR. Mechanisms for the clustering of inertial particles in the inertial range of isotropic turbulence. Phys Rev E 2015;92(2):023029.

[23] Ireland PJ, Bragg AD, Collins LR. The effect of reynolds number on inertial particle dynamics in isotropic turbulence. Part 1. Simulations without gravitational effects. J Fluid Mech 2016;796:617–58.
[24] Hemamalini S, Cuenot B, van Oijen J, Mi X. Numerical study probing the effects of preferential concentration on the combustion of iron particles in a mixing layer. Proc Combust Inst 2024;40(1):105617.
[25] Thäter G, Carbone M, Luu T-D, Stein OT, Frohnapfel B. The influence of clustering in homogeneous isotropic turbulence on the ignition behavior of iron particles. Proc Combust Inst 2024;40(1):105348.
[26] Carbone M, Bragg A, Iovieno M. Multiscale fluid-particle thermal interaction in isotropic turbulence. J Fluid Mech 2018;881:679–721.
[27] Mcbride BJ, Gordon SD, Reno MA. Coefficients for calculating thermodynamic and transport properties of individual species. NASA Langley Research Center; 1993.
[28] Smooke MD. Reduced kinetic mechanisms and asymptotic approximations for methane-air flames. Springer-Verlag Berlin, Heidelberg; 1991.
[29] Rehm RG, Baum HR. The equations of motion for thermally driven, buoyant flows. J Res Natl Bur Stand (1977) 1978;83(3):297–308.
[30] Kumar B, Schumacher J, Shaw RA. Cloud microphysical effects of turbulent mixing and entrainment. Theor Comput Fluid Dyn 2013;27(3):361–76.
[31] Chase M. NIST-JANAF thermochemical tables. 4th ed. American Institute of Physics; 1998.
[32] Ranz W, Marshall W. Evaporation from drops. Chem Eng Prog 1952;48:141–6.
[33] Pope SB. Turbulent flows. Cambridge University Press; 2000.
[34] Steffens P, Hebel J, Braig D, Vahl A, Berkel LL, Schary S, et al. Exploring turbulent methane-assisted iron dust combustion: a combined experimental and numerical study of a 47 kWth lab-scale combustor. Fuel 2025;392:135205.
[35] Monchaux R, Bourgoin M, Cartellier A. Preferential concentration of heavy particles: a Voronoï analysis. Phys Fluids 2010;22(10):103304.
[36] Momenifar M, Bragg AD. Local analysis of the clustering, velocities, and accelerations of particles settling in turbulence. Phys Rev Fluids 2020;5(3):034306.
[37] Ramasubramani V, Dice BD, Harper ES, Spellings MP, Anderson JA, Glotzer SC. Freud: a software suite for high throughput analysis of particle simulation data. Comput Phys Commun 2020;254:107275.
[38] Rycroft CH. Voro++: a three-dimensional Voronoi cell library in C++. Chaos 2009;19(4):041111.
[39] Liu Y, Shen L, Zamansky R, Coletti F. Life and death of inertial particle clusters in turbulence. J Fluid Mech 2020;902:R1.
[40] Hemamalini S, Cuenot B, Mi X. A theoretical analysis of timescales in preferential concentration of burning iron particles, Available at SSRN: https://ssrn.com/abstract=5138232
[41] Lesieur M. Turbulence in fluids. Springer Dordrecht; 2008.
[42] Taylor GI. Diffusion by continuous movements. Proc London Math Soc 1922;s2–20(1):196–212.
[43] Green MS. Markoff random processes and the statistical mechanics of time-dependent phenomena. II. Irreversible processes in fluids. J Chem Phys 1954;22(3):398–413.